Possible nematic spin liquid in spin-1 antiferromagnetic system on the square lattice: Implications for the nematic paramagnetic state of FeSe

Shou-Shu Gong,[1] W. Zhu,[2] D. N. Sheng,[2] and Kun Yang[3]

[1]*National High Magnetic Field Laboratory, Florida State University, Tallahassee, Florida 32310, USA*
[2]*Department of Physics and Astronomy, California State University, Northridge, California 91330, USA*
[3]*National High Magnetic Field Laboratory and Department of Physics, Florida State University, Tallahassee, Florida 32306, USA*

The exotic normal state of iron chalcogenide superconductor FeSe, which exhibits vanishing magnetic order and possesses an electronic nematic order, triggered extensive explorations of its magnetic ground state. To understand its novel properties, we study the ground state of a highly frustrated spin-1 system with bilinear-biquadratic interactions using an unbiased large-scale density matrix renormalization group. Remarkably, with increasing biquadratic interactions, we find a paramagnetic phase between Néel and stripe magnetic ordered phases. We identify this phase as a candidate of nematic quantum spin liquid by the compelling evidences, including vanished spin and quadrupolar orders, absence of lattice translational symmetry breaking, and a persistent nonzero lattice nematic order in the thermodynamic limit. The established quantum phase diagram naturally explains the observations of enhanced spin fluctuations of FeSe in neutron scattering measurement and the phase transition with increasing pressure. This identified paramagnetic phase provides a possibility to understand the novel properties of FeSe.

I. INTRODUCTION

In spin-1/2 antiferromagnets, the interplay between quantum fluctuations and geometric frustration may generate exotic paramagnetic states such as quantum spin liquid [1,2]. With rapidly suppressed quantum fluctuations, it is usually believed that the higher spin system such as spin-1 would favor magnetic order. Interestingly, some spin-1 systems may have additional biquadratic interaction, and the competing interactions can also lead to unusual paramagnetic states such as the Affleck-Kennedy-Lieb-Tasaki (AKLT) state [3,4] and quadrupolar state [5,6]. While these states have been found in both theoretical models and realistic systems, the studies on spin liquid are limited in contrived models [7] and effective field theories [8–11]. The exotic spin liquid has not been found in any realistic microscopic model. Recent exploration of this question [8–11] is further stimulated by spin-1 triangular antiferromagnets $NiGa_2S_4$ [12] and $Ba_3NiSb_2O_9$ [13], which behave like gapless spin liquids in experiments.

In recent studies on iron-based superconductors [14–16], the iron chalcogenide FeSe [17] is attracting much attention because of its paramagnetic normal state, which differs from the conventional magnetic ordered normal states of cuprates [18] and iron pnictides [14–16]. Besides, FeSe possesses an electronic nematic order after a tetragonal-to-orthorhombic structural transition at $T_s \simeq 90$ K [19–22]. Although the primary origin of this nematic order is still unclear [23–34], neutron scattering measurements indicate the important role of spin degree of freedom [24,25]. These novel properties have triggered wide interests in the magnetic ground state of FeSe [35–45]. Neutron experiment finds a large effective spin of $S \simeq 0.74$ [25], which strongly supports the relevance of the spin-1 model as a starting point for understanding the magnetism of FeSe. Along this line, first-principles calculations [36,37,44,46] find that in FeSe the magnetic interactions are highly frustrated and biquadratic interaction

plays an important role [36,37,44]. This naturally leads us to the spin model

$$H = J_{i,j} \sum_{(i,j)} \vec{S}_i \cdot \vec{S}_j + K_{i,j} \sum_{(i,j)} (\vec{S}_i \cdot \vec{S}_j)^2, \quad (1)$$

which contains further-neighbor interactions and is also considered to be relevant to other iron superconductors [47–50]. Semiclassical calculations for this model find various magnetic ordered phases to interpret the observed magnetic orders in iron pnictides and FeTe [36,42,47–52]. Recent mean-field studies propose an antiferroquadrupolar (AFQ) state for FeSe [39,40], which exhibits a nematic order accompanied by the quadrupolar fluctuations at wave vector $\vec{q} = (0,\pi)/(\pi,0)$. While mean-field approach can efficiently detect magnetic and quadrupolar ordered phases, it may not accurately predict the paramagnetic states generated from the frustrated competing interactions in Hamiltonian (1). Such possibilities for FeSe may include the paramagnetic state that might be continuously connected to decoupled spin-1 chains [38,53] and nematic spin liquid [54–56]. To accurately determine the phase diagram of such a strongly frustrated system and uncover quantum phases, unbiased studies are highly desired.

In this article we study the ground state of the frustrated spin-1 model (1) on the square lattice with first- (J_1,K_1) and second-neighbor (J_2,K_2) interactions using unbiased density matrix renormalization group (DMRG) [57]. We set $J_1 = 1.0$ as the energy scale. Considering stripe spin fluctuations in FeSe [23–25] and the first-principles simulation results [36,37], we fix $J_2 = 0.7$ and set $K_1 < 0$. For such a parameter setup, $K_2 < 0$ only enhances ferroquadrupolar (FQ) order [41]; thus we consider $K_2 > 0$. In the semiclassical phase diagram obtained from the site-factorized wave function calculation [58], this system possesses a stripe antiferromagnetic (AFM) and a Néel AFM phase separated by the dash-dot line in Fig. 1(a). In DMRG calculations, through finite-size scaling of magnetic
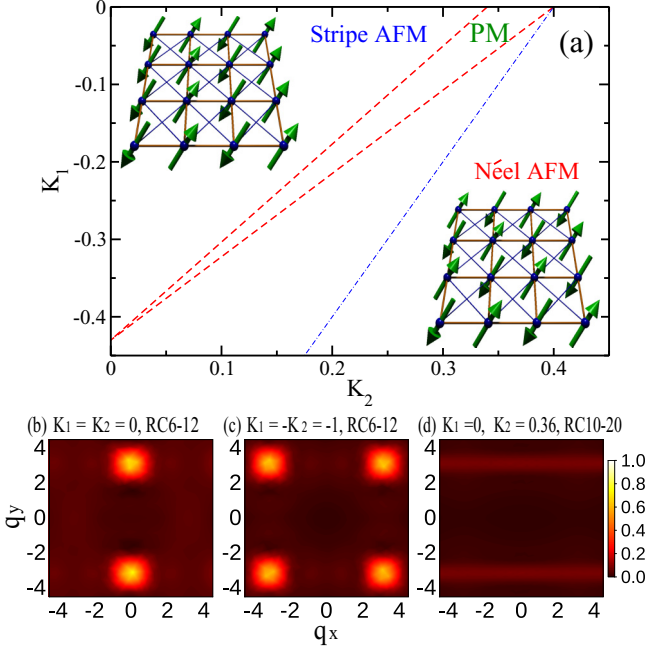
FIG. 1. Different quantum phases in the spin-1 J_1-J_2-K_1-K_2 model on the square lattice. (a) Quantum phase diagram for $J_2 = 0.7$ in the K_1-K_2 plane. With varying K_1 and K_2, the system has a stripe and a Néel AFM phase. Between these two phases, we find a paramagnetic (PM) phase with lattice rotational symmetry breaking, which is between the red dash lines. The blue dash-dot line is the semiclassical phase boundary between the stripe and Néel AFM phase. (b)–(d) Magnetic order parameter $m^2(\vec{q})$ in momentum space for the different phases. In the stripe (b) and Néel phase (c), m^2 has a peak at $\vec{q} = (0,\pi)$ and (π,π), respectively. In the paramagnetic phase, m^2 is featureless as shown in (d).

order parameters, we find a paramagnetic regime sandwiched by the magnetic ordered phases as shown in Fig. 1(a). We identify this phase as a candidate of nematic quantum spin liquid by observing vanished spin and quadrupolar orders, no lattice translational symmetry breaking, and nonzero lattice nematic order in the thermodynamic limit. The neighboring stripe phase can naturally explain the enhanced stripe spin fluctuations in neutron scattering measurement of FeSe [24,25]. This identified paramagnetic phase not only provides a possibility to understand the exotic normal state of FeSe, but also sheds more light on quantum spin liquid in spin-1 magnetic systems.

In our DMRG calculations, we study the rectangular cylinder (RC) system with periodic boundary in the y direction and open boundaries in the x direction. We denote the cylinder as RCL_y − L_x, where L_y and L_x are the number of sites in the y and x directions; the width of the cylinder is $L = L_y$ [see the inset of the RC4-4 cylinder in Fig. 1(a)]. By implementing spin rotational SU(2) symmetry [59], we study cylinder system with L up to 10 by keeping up to 20 000 $U(1)$-equivalent states with truncation error below 1×10^{-5} in most calculations. Our simulations allow us to obtain accurate quantum phase diagram based on different measurements.
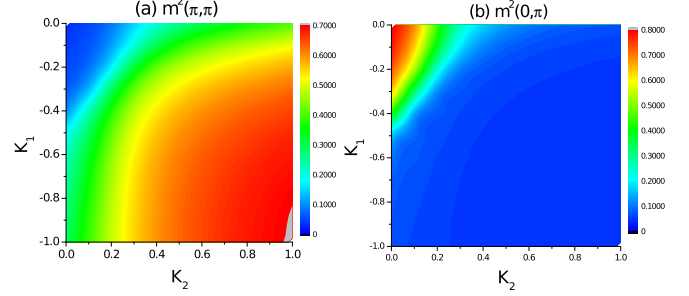

FIG. 2. K_1 and K_2 dependence of magnetic order parameters for the J_1-J_2-K_1-K_2 square model with $J_2 = 0.7$ on the RC6-12 cylinder. (a) and (b) Néel order parameter $m^2(\pi,\pi)$ and stripe order parameter $m^2(0,\pi)$, respectively.

II. MAGNETIC AND QUADRUPOLAR ORDERS

First of all, we show the biquadratic coupling dependence of magnetic order parameters on the RC6-12 cylinder in Fig. 2. For this system, we have $J_2 = 0.7$. With growing K_2, the stripe AFM order at small $|K_1|$ side is suppressed and Néel order develops. In the large $|K_1|$ regime, the Néel order persists with increased K_2. The global picture of Fig. 2 is consistent with the quantum phase diagram Fig. 1(a).

To further study magnetic order, we calculate spin structure factor $m^2(\vec{q}) = \frac{1}{N^2} \sum_{i,j} \langle \vec{S}_i \cdot \vec{S}_j \rangle e^{i\vec{q}\cdot(\vec{r}_i - \vec{r}_j)}$ (N is the total numer of sites) from the spin correlations $\langle \vec{S}_i \cdot \vec{S}_j \rangle$ of the $L \times L$ sites in the middle of the RC$L − 2L$ cylinder, which efficiently reduces edge effects of open cylinder [60–62]. In the stripe and Néel AFM states, $m^2(\vec{q})$ has the characteristic peak at $\vec{q} = (0,\pi)/(\pi,0)$ and (π,π), respectively; these are shown in Figs. 1(b) [the stripe state selects the peak at $(0,\pi)$ because of the cylinder geometry] and 1(c). In the intermediate regime, $m^2(\vec{q})$ is featureless as shown in Fig. 1(d). Compared with the semiclassical phase boundary, one finds that our DMRG phase boundaries shift dramatically to the small K_2 side, where the semiclassical calculations may overestimate the stripe order. In Figs. 3(a) and 3(b) we show $m^2(0,\pi)$ and $m^2(\pi,\pi)$ for $K_1 = 0.0$ with growing K_2 and $L = 4$–10. The appropriate finite-size scaling suggests that the stripe order vanishes at $K_2 \simeq 0.34$, and the Néel order develops at $K_2 \simeq 0.4$, leaving an intermediate regime with no magnetic order. The log-log plots of magnetic orders versus system width are shown in Figs. 3(c) and 3(d), where both orders appear to vanish in a power-law manner in the intermediate regime. Thus we establish a paramagnetic phase in this regime, possibly with critical magnetic fluctuations. To demonstrate the stability of the intermediate phase, we examine the extended parameter regime with $J_2 = 0.75, 0.8$ and we also identify the intermediate phase by tuning biquadratic coupling (see Appendix A), which supports a stable nonmagnetic phase. Next, we will demonstrate various measurement results to characterize the physics in the intermediate phase.

Since biquadratic interaction is present in the system, we investigate the quadrupolar order $\mathbf{Q}_i$ [5,6], where $\mathbf{Q}_i = (Q_i^{3z^2-r^2}, Q_i^{x^2-y^2}, Q_i^{xy}, Q_i^{yz}, Q_i^{zx})$ is a rank-two tensor operator with five components $Q_i^{3z^2-r^2} = [2(S_i^z)^2 - (S_i^x)^2 - (S_i^y)^2]/\sqrt{3}$, $Q_i^{x^2-y^2} = (S_i^x)^2 - (S_i^y)^2$, $Q_i^{xy} = S_i^x S_i^y + S_i^y S_i^x$,
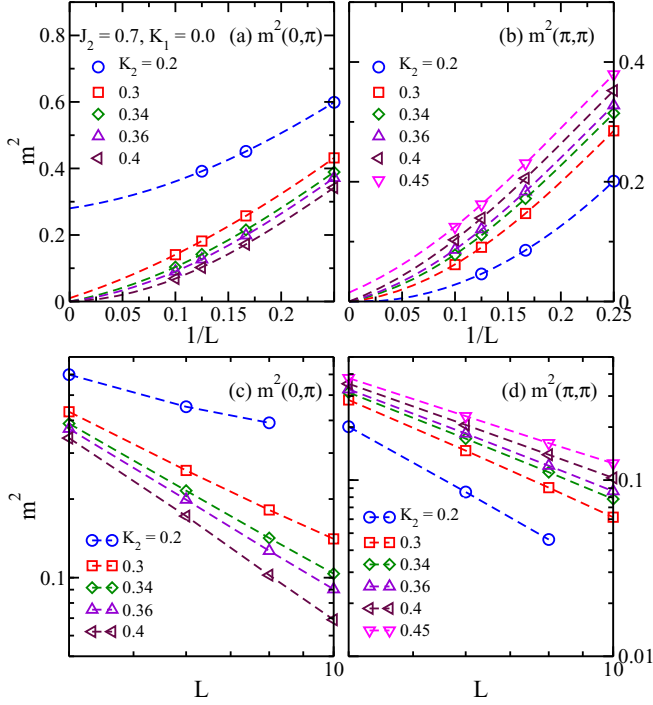
FIG. 3. Finite-size scaling of magnetic order parameters. (a) and (b) Size extrapolations of stripe order $m^2(0,\pi)$ and Néel order $m^2(\pi,\pi)$ versus $1/L$, respectively. We have the system with $J_2 = 0.7, K_1 = 0.0$ on the RC$L - 2L$ cylinders with $L = 4$–10. Dashed lines are polynomial fits up to fourth order. (c) and (d) Log-log plots of the two magnetic orders versus width L.
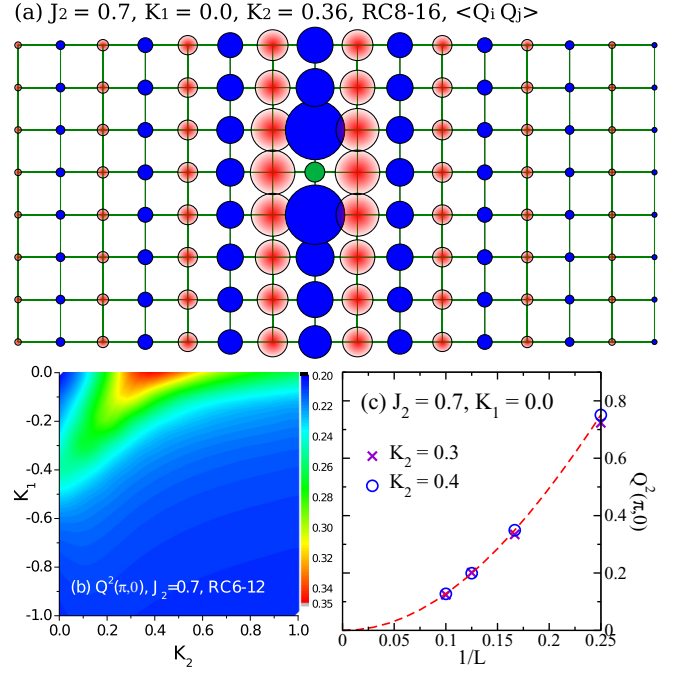

FIG. 4. The absence of stripe AFQ order. (a) Stripe $(\pi,0)$ AFQ correlation $\langle \mathbf{Q}_i \cdot \mathbf{Q}_j \rangle$ for $J_2 = 0.7, K_1 = 0.0, K_2 = 0.36$ on the RC8-16 cylinder. The solid green circle in the middle denotes the reference site. The solid blue and shaded red circles denote the positive and negative AFQ correlations, respectively. (b) K_1, K_2 dependence of stripe AFQ order parameter $Q^2(\pi,0)$ on the RC6-12 cylinder. (c) Finite-size scaling of $Q^2(\pi,0)$ up to width $L = 10$.

$Q_i^{yz} = S_i^y S_i^z + S_i^z S_i^y$, and $Q_i^{zx} = S_i^z S_i^x + S_i^x S_i^z$. In Fig. 4(a) we show that the quadrupolar correlation in the intermediate regime exhibits a stripe AFQ pattern. To detect stripe AFQ order, we calculate quadrupolar structure factor $Q^2(\vec{q}) = \frac{1}{N^2} \sum_{i,j} \langle \mathbf{Q}_i \cdot \mathbf{Q}_j \rangle e^{i\vec{q} \cdot (\vec{r}_i - \vec{r}_j)}$ defined in a way similar to $m^2(\vec{q})$. In Fig. 4(b) we show the stripe AFQ order parameter $Q^2(\pi,0)$ on the RC6-12 cylinder in the K_1-K_2 plane, where the finite-size $Q^2(\pi,0)$ is enhanced in the intermediate regime. However, the size extrapolation in Fig. 4(c) shows that $Q^2(\pi,0)$ approaches zero for $L \to \infty$, indicating the vanishing AFQ order in the thermodynamic limit.

III. NEMATIC ORDER

Next, we study lattice symmetry breaking by measuring the nearest-neighbor J_1 bond energy $\langle \vec{S}_i \cdot \vec{S}_j \rangle$. In Fig. 5(a) we show the bond energy for $K_1 = 0.0, K_2 = 0.36$ on the RC8-16 cylinder, which is quite translationally uniform in the bulk of cylinder. Note that the open boundary conditions in the x direction of the cylinder system usually induce a bond translational symmetry breaking, and the corresponding dimer order (the bond energy difference along the x direction $\langle \vec{S}_i \cdot \vec{S}_{i+1} \rangle - \langle \vec{S}_{i+1} \cdot \vec{S}_{i+2} \rangle$) decays from the edge to the bulk. For a valence-bond crystal (VBC) phase, the dimer order decay length would increase fast while in a non-VBC phase the decay length is finite in the thermodynamic limit [63]. In our DMRG calculations, we find that the bond dimer order always decays

quite fast with a very short decay length on our studied system size, indicating the preserved lattice translational symmetry.

Importantly, one can see a strong nematicity between horizontal and vertical bond energy. We define a bond nematic order as $\sigma_1 \equiv \langle \vec{S}_i \cdot \vec{S}_{i+\hat{x}} \rangle - \langle \vec{S}_i \cdot \vec{S}_{i+\hat{y}} \rangle$ with the bond energy in the bulk of the cylinder. Note that here the bond energy is not translationally invariant only for few columns on the edge. σ_1 versus $1/L$ is presented in Fig. 5(b) for different K_2. We show the cylinder length dependence of σ_1 in the inset of Fig. 5(b), which indicates the extremely small finite-size effects of σ_1 versus L_x. In the stripe AFM phase for $K_2 \lesssim 0.34$, σ_1 scales to finite value with $1/L$, supporting the rotational symmetry breaking of stripe magnetic ordered phase. For $K_2 > 0.4$, σ_1 decreases fast and tends to vanish, which strongly indicates a transition to a phase without lattice rotational symmetry breaking. This transition is compatible with the developing Néel order at $K_2 \simeq 0.4$ found in Fig. 3(b). Interestingly, in the intermediate phase, we find that the nematic order also decreases slowly and approaches a finite value for $L \to \infty$, indicating lattice rotational symmetry breaking in this intermediate phase.

We remark that the finite nematic order observed in the intermediate phase is not induced by cylinder geometry but intrinsic. For the geometry induced nematic order such as the order in the neighboring Néel phase without a C_4 symmetry breaking, one can see that the order decays very fast to vanish with growing cylinder width, in contrast to the scaling behavior in the intermediate phase. As a numerical method, we would
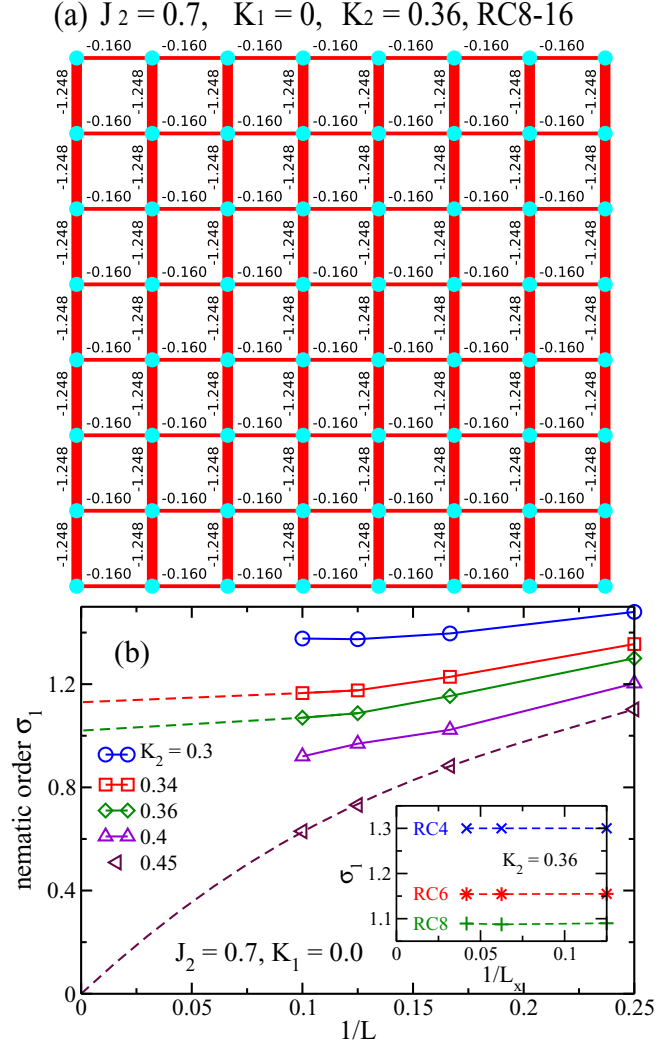
FIG. 5. Lattice symmetry breaking in the intermediate phase. (a) J_1 bond energy $\langle \vec{S}_i \cdot \vec{S}_j \rangle$ for $K_1 = 0.0, K_2 = 0.36$ on the RC8-16 cylinder. Here we only show the middle 8×8 sites. (b) Finite-size scaling of bond nematic order σ_1. The inset shows the cylinder length dependence of σ_1 for $K_2 = 0.36$ and different L_y.

like to point out that for detecting lattice symmetry breaking, edge bond pinning has been shown effective in quantum Monte Carlo [63] and DMRG simulations [61,62,64]. In the recent DMRG calculations for the spin-1/2 J_1-J_2 triangular Heisenberg model [65–67], a strong nematic order is also found, which is considered as an evidence of a spontaneous rotational symmetry breaking of the identified spin liquid phase.

IV. SPIN GAP

The vanishing magnetic order and spontaneous lattice rotational symmetry breaking suggest the intermediate phase as a possible AKLT state [38] or a nematic spin liquid. To further characterize this phase, we calculate the finite-size spin-1 excitation gap, defined as the energy difference between the lowest energy states in total spin-1 and spin-0 sectors for a given system size [62,68,69]. We demonstrate spin gap with
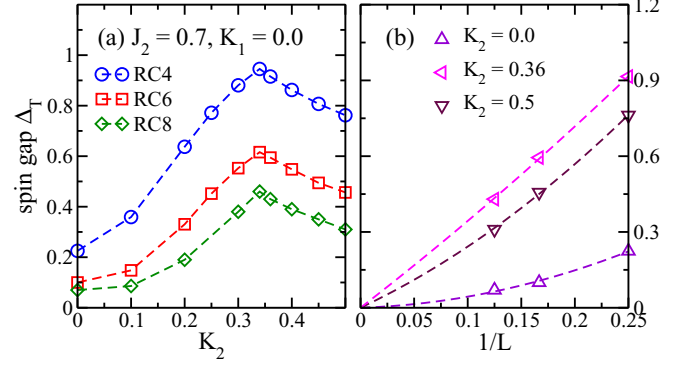

FIG. 6. Spin gap Δ_T in the different phases. (a) Δ_T versus K_2 for $J_1 = 0.7, K_1 = 0.0$ on different cylinders. (b) Finite-size scaling of spin gap Δ_T in different phases. To avoid edge excitations, spin gap is obtained by sweeping the middle $L \times L$ sites with total spin $S = 1$ based on the ground state of the long RC$L - L_x$ cylinders with $L_x = 24$ and $L = 4,6,8$.

increasing K_2 in Fig. 6(a), where it exhibits a kink at $K_2 = 0.34$. While the ground-state energy varies smoothly with growing K_2 (see Appendix A), the kink of spin gap indicates an energy level crossing in the spin-1 sector, which could be compatible with the phase transition found in Fig. 3(a). At $K_2 = 0.4$, both ground-state energy and spin gap exhibit no singularity on our studied system size, which suggest a possible continuous phase transition. The vanishing nematic order for $K_2 \gtrsim 0.4$ and the spin gap singularity at $K_2 = 0.34$ support the intermediate phase found in the finite-size scaling of magnetic orders.

In Fig. 6(b) we show finite-size scaling of the spin gap in different phases. In both stripe and Néel phases, spin gap is smoothly scaled to zero, which agrees with the gapless spin excitations from continuous spin rotational symmetry breaking. In the paramagnetic phase, the spin gap also approaches zero appropriately, which seems to be inconsistent with a spin gapped AKLT-like state [38] but leaves a possibility of a gapless nematic spin liquid.

V. DMRG RESULTS ON THE TILT CYLINDER

As a supplementary of our finite-size calculations, we also test the tilted cylinder (TC) that is obtained by a $\pi/4$ rotation of the rectangular lattice. A schematic figure of the TC cylinder is shown in Fig. 7. The cylinder width for the TC cylinder is $W_y = \sqrt{2}L_y$. It should be noticed that different from RC, the bond $\pi/2$ rotational symmetry is not broken by geometry on the TC cylinder.

First of all, we calculate the spin order on the TC cylinder. We find the consistent $(0,\pi)$ and (π,π) magnetic orders in the small K_2 and large K_2 regimes, respectively. However, in the intermediate K_2 regime where we find a nonmagnetic state on the RC cylinder, DMRG calculations obtain a state with strong spin correlations on the TC cylinder. As shown in Fig. 8, while the spin correlations on the RC cylinder decay exponentially to vanish, those on the TC cylinder decay quite slowly, which does not support a nonmagnetic state.
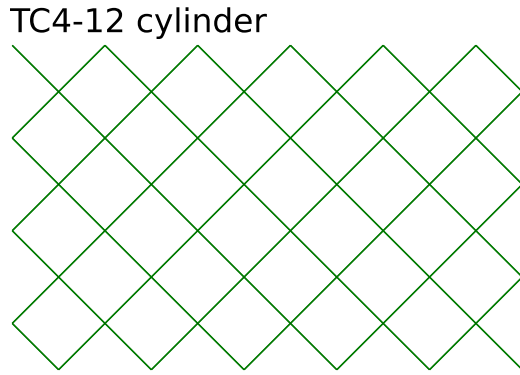
TC4-12 cylinder

FIG. 7. A schematic figure for the 45-deg tilted cylinder (TC) on the square lattice. Here the cylinder width is $L_y = 4$ and the length is $L_x = 12$, which is denoted as TC4-12. For the TC cylinder, the cylinder width is $\sqrt{2}L_y$.

To understand the different results on the two geometries, we compare the bulk energy on both systems. As shown in Fig. 9, in the two magnetic order phases, the bulk energies on both geometries approach each other with increasing cylinder width, indicating the consistent energy in large size limit. However, in the intermediate regime, the TC cylinder appears to have a higher energy than the RC cylinder. The close energies of the two states may imply the gapless nature of the low-lying excitations, which is consistent with the vanishing gap in the intermediate phase. The lower energy of the nonmagnetic state supports it as the stronger candidate of the true ground state. We also remark that in our DMRG calculations on the TC cylinder, convergence is very challenging and the DMRG truncation error is much bigger than the RC cylinder with the similar W_y, which suggests that the TC cylinder may not be a proper geometry for studying the intermediate phase.

VI. DISCUSSION AND SUMMARY

Motivated by the exotic nematic paramagnetic normal state of iron chalcogenide superconductor FeSe, we study a spin-1 J_1-J_2-K_1-K_2 system on the square lattice using a density matrix renormalization group. By implementing spin rotational SU(2) symmetry, we study cylinder geometry with system width up to 10 legs, which significantly reduces finite-size
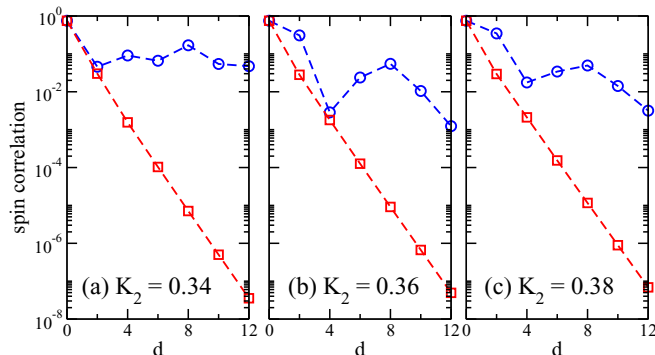

FIG. 8. Log-linear plots of the spin correlations in the intermediate K_2 regime for $J_2 = 0.7, K_1 = 0.0$ on the RC6 and TC4 cylinders. The red squares denote the RC6 cylinder, and the blue circles denote the TC4 cylinder.
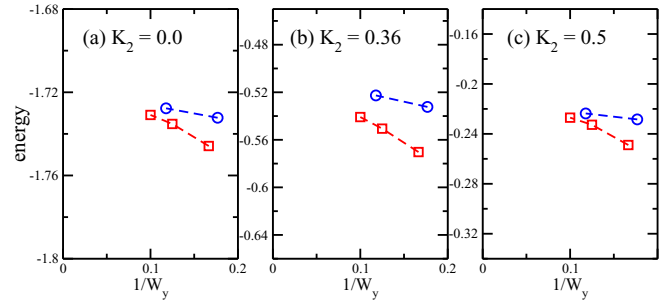

FIG. 9. Bulk energy versus cylinder width W_y on the RC and TC cylinders. The system has $J_2 = 0.7, K_1 = 0.0$ and different K_2. For (a) $K_2 = 0.0$, the system is in the $(0,\pi)$ magnetic order phase. For (b) $K_2 = 0.36$, the system is in the intermediate regime. For (c) $K_2 = 0.5$, the system is in the (π,π) magnetic order phase. The blue circles are the bulk energy for the RC6, RC8, and RC10 cylinders. The red squares denote the energy for the TC4 and TC6 cylinders. For the RC cylinder, cylinder width $W_y = L_y$; for the TC cylinder, $W_y = \sqrt{2}L_y$. In the two magnetic order phases, the energies on the two geometries approach each other. However, in the intermediate regime, the TC cylinder appears to have the higher energy than the RC cylinder on our studied system size.

effects of order parameter scaling. With increased biquadratic interactions K_1, K_2, we find a paramagnetic phase between stripe and Néel magnetic ordered phases, which preserves all spin rotational and lattice translational symmetries but breaks lattice rotational symmetry.

The nematic paramagnetic state in this J_1-J_2-K_1-K_2 system provides a possibility to understand the magnetic ground state of FeSe. The current findings naturally match the observations of FeSe in neutron scattering [24,25] and high pressure experiments [31–33], where the paramagnetic state of FeSe with substantial stripe spin fluctuations is identified to sit close to the stripe magnetic phase and may undergo a phase transition to the stripe magnetic ordered phase at high pressure. As FeSe is a bad metal that is in proximity of a Mott insulator, it would be interesting to consider the effects of itinerant electrons on the nematicity of the localized moments in further study. Our DMRG results suggest this paramagnetic state may be a nematic quantum spin liquid. Spin liquid states in spin-1 system have been discussed for the triangular antiferromagnets [8–11] related to materials $NiGa_2S_4$ [12] and $Ba_3NiSb_2O_9$ [13], but have not been found in unbiased calculations besides our work. Our work provides insight for the interplay between spin Heisenberg and biquadratic interactions, and sheds more light on interesting phases in spin-1 system.
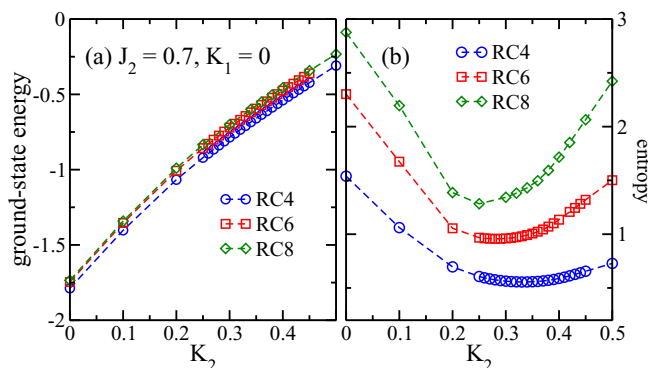
FIG. 10. K_2 coupling dependence of (a) ground-state energy and (b) entanglement entropy for $J_2 = 0.7, K_1 = 0.0$ in different long cylinders with $L_x = 24$.

APPENDIX A: J_1-J_2-K_1-K_2 SQUARE MODEL

In Fig. 10 we show the K_2 coupling dependence of the ground-state energy and entanglement entropy in the bulk of cylinder for $J_2 = 0.7, K_1 = 0.0$ on different cylinders. In the main text, we show that the system has an intermediate phase for $0.34 \lesssim K_2 \lesssim 0.4$. Here we find that both the ground-state energy and the entropy appear smooth near the phase boundaries, which indicates possible continuous transitions. Generally, a direct phase transition from Néel to stripe AFM phase would be first order in Landau's paradigm. The smooth transition behaviors could be compatible with an intermediate paramagnetic phase between the two magnetic ordered phases.

To demonstrate the stability of the intermediate phase, we also extend the studied parameter regime to $J_2 = 0.75$ and 0.8. Following the setup for $J_2 = 0.7$, we fix $K_1 = 0.0$ and tune K_2. In Figs. 11 and 12 we show the magnetic spin dipole structure factor $S(q) = \frac{1}{N} \sum_{i,j} e^{iq \cdot (r_i - r_j)} \langle S_i \cdot S_j \rangle$ on the RC8-16 cylinder. For $J_2 = 0.75$, one can find that the spin structure factor is featureless for $0.48 \lesssim K_2 \lesssim 0.6$; and for $J_2 = 0.8$, the structure factor is featureless for $0.6 \lesssim K_2 \lesssim 0.75$. In the nonmagnetic intermediate regime for $J_2 = 0.75, 0.8$, we also examine the quadrupolar order (not shown here), which exhibits the same $(\pi, 0)$ AFQ fluctuations as we find for $J_2 = 0.7$ in the intermediate phase. In Fig. 13 we also show the finite-size scaling of the nematic order $\sigma_1 \equiv \langle \vec{S}_i \cdot \vec{S}_{i+\hat{x}} \rangle - \langle \vec{S}_i \cdot \vec{S}_{i+\hat{y}} \rangle$ in the intermediate regime for $J_2 = 0.75$ and 0.8. Consistently, the size scaling also indicates the finite nematic order. Therefore, our results indicate that the nonmagnetic nematic intermediate phase is stable by tuning J_2.

APPENDIX B: J_1-J_2-K_1 SQUARE MODEL

Magnetic orders. We show the magnetic order parameters on the RC6-12 cylinder for $0.5 \leqslant J_2 \leqslant 1.0, 0.5 \leqslant |K_1| \leqslant 1.0$ in Fig. 14. We find that the stripe AFM order develops very fast above a critical J_2. This phase transition is denoted by the red dash line in Fig. 14. For the Néel phase, we can find that the blue regime with weak Néel order before the transition to stripe phase in Fig. 14(a) is enlarged with increasing $|K_1|$, which may indicate an intermediate regime.
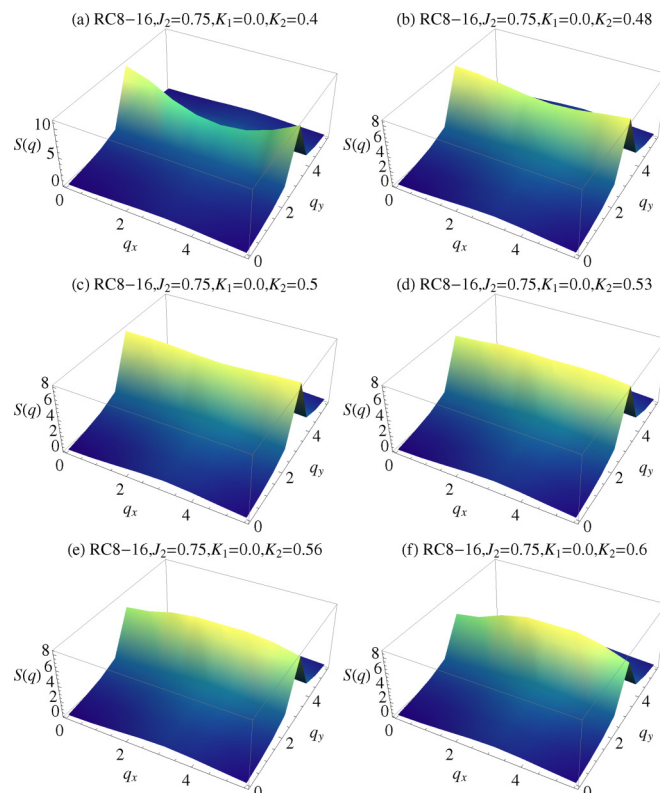

FIG. 11. Spin structure factor $S(\vec{q})$ for $J_2 = 0.75, K_1 = 0.0$ and different K_2 on the RC8-16 cylinder. The structure factor is obtained by the Fourier transform from the spin correlations of the middle 8×8 sites. For $K_2 = 0.4$, $S(\vec{q})$ has the stripe characteristic peak at $\vec{q} = (0, \pi)$. For $0.48 \lesssim K_2 \lesssim 0.6$, $S(\vec{q})$ is featureless, consistent with the nonmagnetic intermediate phase.

To determine whether there is an intermediate phase, we make finite-size scaling of magnetic order parameters. In Fig. 15 we show the size scaling of Néel and stripe order parameters for $K_1 = -0.8$ with increased J_2. Here, as the convergence challenge in DMRG calculations in the intermediate regime, we only show the data up to $L = 8$. Through the appropriate extrapolation, we find that the Néel order vanishes at $J_2 \simeq 0.75$ and the stripe order develops at $J_2 \simeq 0.88$, which give us the transition points shown in Fig. 14(a) and identify an intermediate paramagnetic phase.

Ferroquadrupolar phase. Next we study ferroquadrupolar (FQ) order in the intermediate phase. In Fig. 16(a) we show the J_2, K_1 coupling dependence of the FQ order parameter $Q^2(0,0)$ on the RC6-12 cylinder. We can find the strong enhancement of $Q^2(0,0)$ in the large $J_2, |K_1|$ regime, which is consistent with the intermediate regime identified by studying magnetic orders in Fig. 14. In Fig. 16(b) we show the finite-size scaling of the FQ order, which unambiguously shows the finite FQ order in the thermodynamic limit. Thus, the vanished magnetic order and finite FQ order identify this intermediate regime as a FQ phase.

Preserved lattice symmetry. We also calculate the nearest-neighbor bond energy $\langle \vec{S}_i \cdot \vec{S}_j \rangle$ to detect lattice symmetry breaking. We find that the bond energy is quite uniform in the bulk of the cylinder, indicating the translational invariance. In Fig. 16(c) we demonstrate the size scaling of the bond nematic
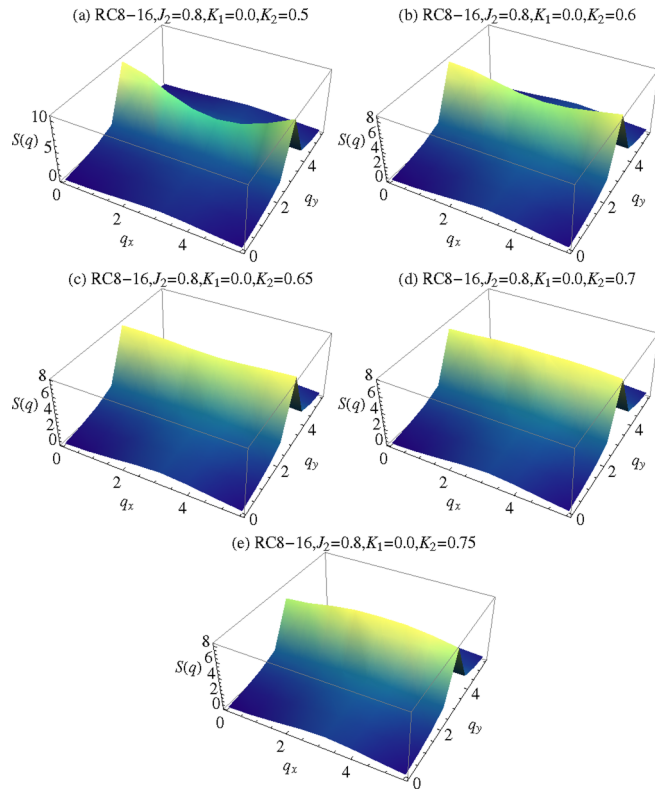
FIG. 12. Spin structure factor $S(\vec{q})$ for $J_2 = 0.8, K_1 = 0.0$ and different K_2 on the RC8-16 cylinder. We obtain the data following the way described in the caption of Fig. 11. Here, for $J_2 = 0.8$, we also find the featureless $S(\vec{q})$ for $0.6 \lesssim K_2 \lesssim 0.75$.

order σ_1 for $K_1 = -0.8$. Similar to the main text, the nematic order σ_1 is defined as the difference between the horizontal and vertical bond energy as $\sigma_1 = \langle \vec{S}_i \cdot \vec{S}_{i+\hat{x}} \rangle - \langle \vec{S}_i \cdot \vec{S}_{i+\hat{y}} \rangle$. While σ_1 is strong and scales to finite value in the stripe AFM phase for $J_2 \gtrsim 0.88$, it decays very fast to vanish in both the Néel and FQ phases.
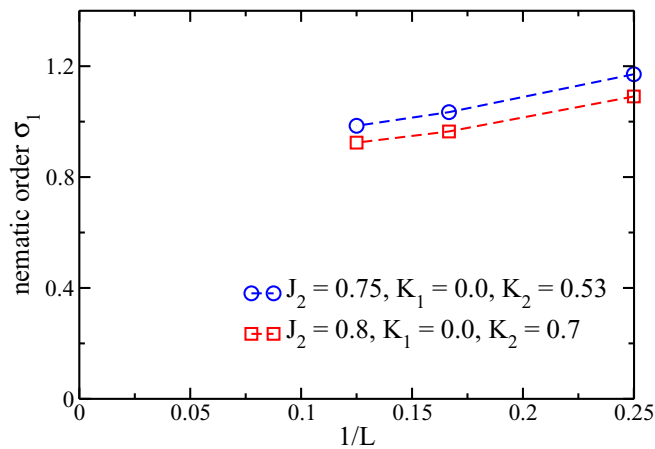

FIG. 13. Size dependence of lattice nematic order σ_1 for the parameter points in the intermediate phase regime for $J_2 = 0.75, 0.8, K_1 = 0.0$.
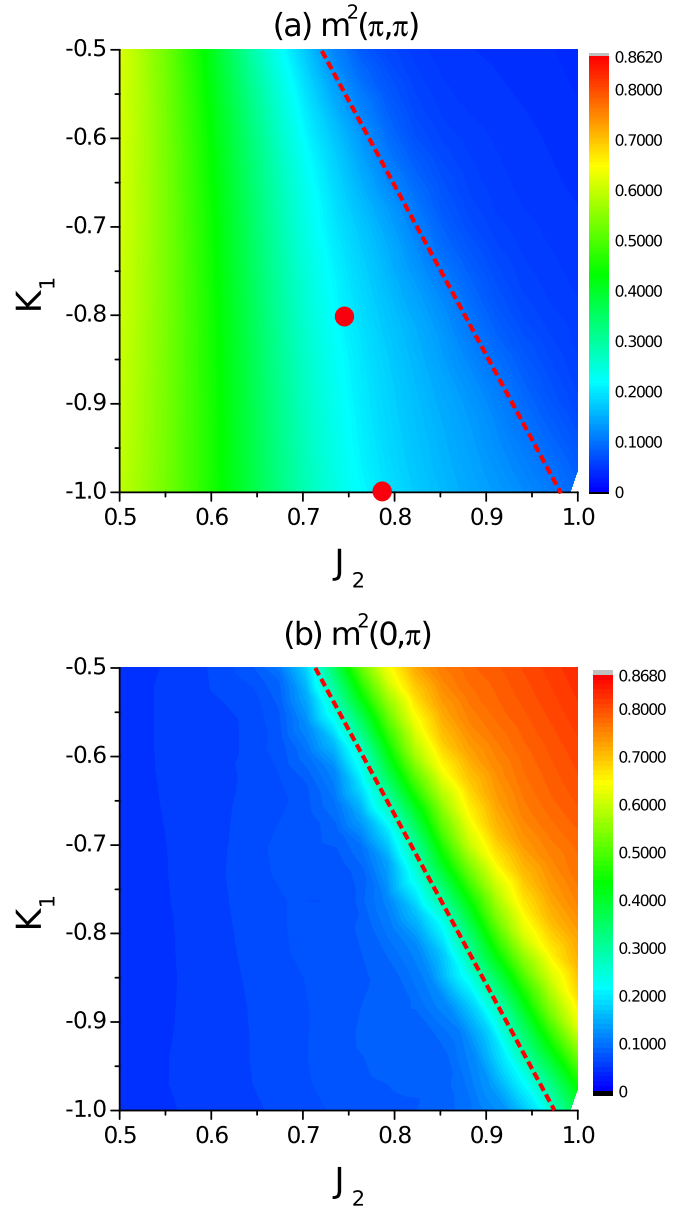

FIG. 14. Néel AFM order parameter $m^2(\pi, \pi)$ (a) and stripe AFM order parameter $m^2(0, \pi)$ (b) versus J_2 and K_1 interactions for the J_1-J_2-K_1 square model on the RC6-12 cylinder. In both figures, the red dash line denotes the phase transition to the stripe AFM order. The red dots in (a) denote the phase transition from Néel to the intermediate ferroquadrupolar phase, which are determined from the finite-size scaling of magnetic order parameters as shown in Fig. 15.

APPENDIX C: ORIGIN OF BIQUADRATIC INTERACTION

We briefly discuss the origin of biquadratic coupling in our model. Generally speaking, there are two different mechanisms to generate biquadratic interaction. One is spin-phonon coupling or lattice distortion effect. The other one is microscopic description of the isotropic non-Heisenberg Hamiltonian extracted at the fourth order of perturbation from a Hubbard Hamiltonian.
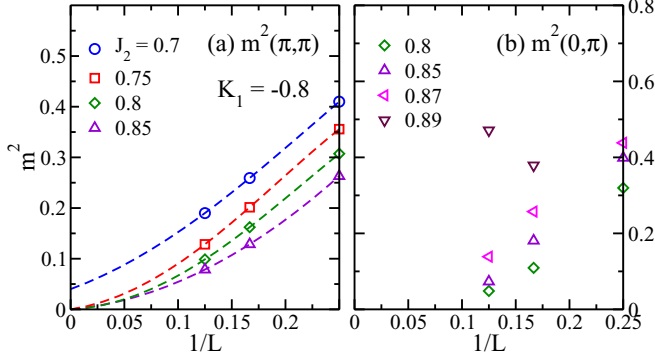
FIG. 15. Finite-size scaling of magnetic order parameters for the J_1-J_2-K_1 square model on the RC$L-2L$ cylinders with $L = 4, 6, 8$. (a) and (b) Néel and stripe magnetic order parameters $m^2(\pi, \pi)$ and $m^2(0, \pi)$ versus $1/L$, respectively. Lines are polynomial fits.

1. Phonon coupling

As a phenomenological origin, one might think of the coupling between spin and lattice degrees of freedom that results from the exchange integrals on the atomic positions in a crystal. Since the exchange integrals are linear functions of the displacement coordinates, while the elastic energy of the deformation shows quadratic behavior, a frustrated system may gain energy by distorting the lattice. Alternatively, the competition between the lattice distortion and the associated energy gain may lead to a quadratic coupling. This effect is discussed in detail for the case of a single tetrahedral molecule with four spins [71]. If we assume that the exchange integral for a pair of neighborhood spins S_i and S_j depends only on

FIG. 16. FQ phase in the J_1-J_2-K_1 model. (a) J_2, K_1 dependence of FQ order parameter $Q^2(0,0)$ on RC6-12 cylinder. (b) Finite-size scaling of $Q^2(0,0)$ in different phases. (c) Finite-size scaling of lattice nematic order σ_1 for $K_1 = -0.8$ and different J_2.

the interatomic distance r_{ij} (a reasonable assumption for direct exchange), the elastic energy associated with a bond distortion can be written as $\kappa \delta r_{ij}^2/2$, where δr_{ij} is the variation of the bond length and κ is the elastic constant. Thus we reach the so-called bond-phonon model:

$$H^{\text{bp}} = J \sum_{ij}(1 - \alpha \delta r_{ij})S_i \cdot S_j + \kappa \delta r_{ij}^2/2, \quad \text{(C1)}$$

where α is the spin-lattice coupling constant. Considering δr_{ij} as independent parameters, we may integrate them out and find an effective spin Hamiltonian:

$$H = J \sum_{\langle i,j \rangle} S_i \cdot S_j + K \sum_{\langle i,j \rangle}(S_i \cdot S_j)^2, \quad \text{(C2)}$$

where $K = -J\alpha/2\kappa$ is a dimensionless constant. Here, based on the bond-phonon model, we get a quadratic interaction in addition to the original Heisenberg spin exchange coupling, despite that this derivation is a semiclassic description [72].

2. Microscopic origin from the Hubbard model

We will derive an effective Hamiltonian for an iron-based superconductor based on simple arguments. Since iron-based superconductors have six electrons occupying the nearly degenerate 3d Fe orbitals, the system is intrinsically multiorbital in a microscopic Hamiltonian. Band structure calculations on iron-based superconductors have shown the primary Fe orbitals are d_{xz}, d_{yz}, and d_{xy}. Based on the further approximation that the role of the d_{xy} can be replaced by a next-near-neighbor hybridization between d_{xz} and d_{yz} orbitals, we get a two-dimensional square lattice with two degenerated d_{xz} and d_{yz} orbitals per site, which is proposed as a minimal two-band model for an iron-based superconductor [73]. The itinerant electrons of the degenerated d_{xz} and d_{yz} orbitals are described by a tight-binding Hamiltonian

$$H = H_t + H_{\text{intra}} + H_{\text{inter}} + H_{\text{Hund}}. \quad \text{(C3)}$$

The itinerant electrons of the degenerate d_{xz} and d_{yz} orbitals are described by a tight-binding Hamiltonian

$$H_t = \sum_{(ij),(\alpha\beta),\sigma} t_{ij,\alpha\beta} c_{i,\alpha,\sigma}^{\dagger} c_{j,\beta,\sigma} + \text{H.c.}, \quad \text{(C4)}$$

where $c_{i,\alpha,\sigma}^{\dagger}$ creates an electron with spin σ at site i on orbital $\alpha = d_{xz(yz)}$. For simplicity we first assume $t_{ij,\alpha\alpha} = t$ for nearest neighbors. We define the intraband Hubbard interaction H_U and interband Hubbard interaction H_V as

$$H_{\text{intra}} = U \sum_{i,\alpha} n_{i,\alpha,\uparrow} n_{i,\alpha,\downarrow}, \quad \text{(C5)}$$

$$H_{\text{inter}} = V \sum_{i,\sigma,\sigma'} n_{i,\alpha,\sigma} n_{i,\beta,\sigma'}, \quad \text{(C6)}$$

and the Hund's rule coupling as

$$H_{\text{Hund}} = -J_H \sum_{i,\alpha,\beta}[c_{i,\alpha,\uparrow}^{\dagger} c_{i,\alpha,\downarrow} c_{i,\beta,\downarrow}^{\dagger} c_{i,\beta,\uparrow} + \text{H.c.}], \quad \text{(C7)}$$
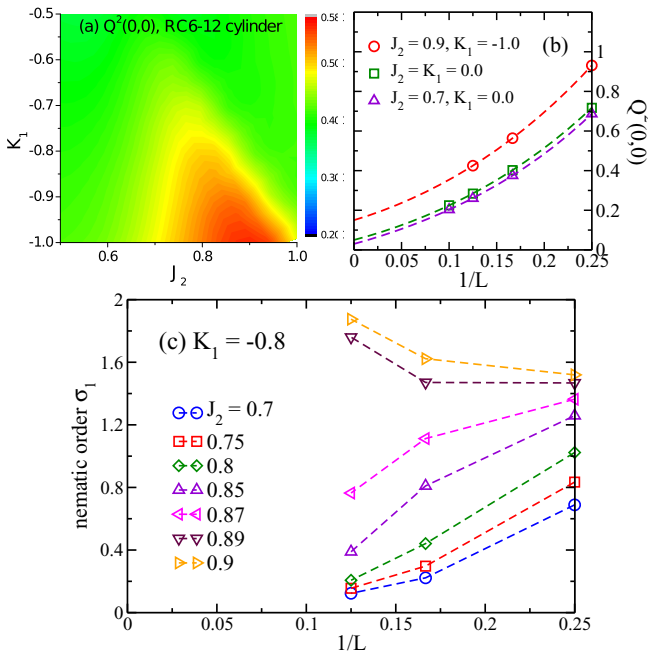
where the Hund coupling ensures that two electrons form a spin triplet if they occupy different orbitals on the same site.

To derive an effective Hamiltonian, let us first consider the limit of strong interaction defined by $U \neq 0$, $J_H \neq 0$, and $t = 0$. For one site, the ground-state manifold is spanned by configurations with two electrons on each site, one in each orbital, and the two electrons of a given site forming a triplet. Thus, the spin-1 model is likely suitable to describe the iron-based superconductor, which also matches the very

recent neutral scattering measurements on FeSe samples [25]. Next we consider two sites. Two $S = 1$ spins can be combined into a total $S = 2, 1, 0$ with the corresponding levels fivefold and threefold degenerate, and nondegenerated, where we label as $|S, S^z\rangle$ and the total spin S and its a-component S^z are good quantum numbers. When a small hopping t is added, the fluctuations will lift the ground-state degeneracy and favor the spin singlet state. Here the discussion is parallel to the case of the simple e_g molecule with two orbitals in each site [74]. We just quote the results, up to fourth-order perturbation $\propto t^4$:

$$H_{\text{eff}} = \left(\frac{2t^2}{U + J_H} - \frac{8t^4}{(U + J_H)^3} \right) S_i \cdot S_j + \frac{12t^4}{(U + J_H)^3} \left(\frac{1}{U + J_H} - \frac{2}{2(U + V) + J_H} - \frac{2}{2(U - V) + J_H} \right) P_{S=0}, \quad \text{(C8)}$$

where S_i is spin-1 operator and $P_{S=0}$ projects to the spin single state:

$$P_{S=0} = \tfrac{1}{3}[(S_i \cdot S_j)^2 - 1]. \quad \text{(C9)}$$

Finally, we get the bilinear-biquadratic exchange Hamiltonian as

$$H_{\text{eff}} = J \sum_{\langle i,j \rangle} S_i \cdot S_j + K \sum_{\langle i,j \rangle} (S_i \cdot S_j)^2. \quad \text{(C10)}$$

For an isolated Fe atom, the intraband interaction U and interband interaction V are similar in magnitude, while Hund

coupling J_H is an order smaller. Thus, a reasonable estimate is $J > 0$ and $K < 0$ for an iron-based superconductor. This model can be also extended to the next-nearest neighbors, thus we have the J_1-J_2-K_1-K_2 model as the start point

$$H_{\text{eff}} = J_1 \sum_{\langle i,j \rangle} S_i \cdot S_j + J_2 \sum_{\langle\langle i,j \rangle\rangle} S_i \cdot S_j$$
$$+ K_1 \sum_{\langle i,j \rangle} (S_i \cdot S_j)^2 + K_2 \sum_{\langle\langle i,j \rangle\rangle} (S_i \cdot S_j)^2. \quad \text{(C11)}$$

[1] L. Balents, Nature (London) **464**, 199 (2010).
[2] L. Savary and L. Balents, Rep. Prog. Phys. **80**, 016502 (2016).
[3] I. Affleck, T. Kennedy, E. H. Lieb, and H. Tasaki, Phys. Rev. Lett. **59**, 799 (1987).
[4] I. Affleck, T. Kennedy, E. H. Lieb, and H. Tasaki, Commun. Math. Phys. **115**, 477 (1988).
[5] M. Blume and Y. Y. Hsieh, J. Appl. Phys. **40**, 1249 (1969).
[6] A. Läuchli, F. Mila, and K. Penc, Phys. Rev. Lett. **97**, 087205 (2006).
[7] H. Yao and S. A. Kivelson, Phys. Rev. Lett. **99**, 247203 (2007).
[8] T. Grover and T. Senthil, Phys. Rev. Lett. **107**, 077203 (2011).
[9] C. Xu, F. Wang, Y. Qi, L. Balents, and M. P. A. Fisher, Phys. Rev. Lett. **108**, 087204 (2012).
[10] S. Bieri, M. Serbyn, T. Senthil, and P. A. Lee, Phys. Rev. B **86**, 224409 (2012).
[11] H.-H. Lai, Phys. Rev. B **87**, 205131 (2013).
[12] S. Nakatsuji, Y. Nambu, H. Tonomura, O. Sakai, S. Jonas, C. Broholm, H. Tsunetsugu, Y. Qiu, and Y. Maeno, Science **309**, 1697 (2005).
[13] J. G. Cheng, G. Li, L. Balicas, J. S. Zhou, J. B. Goodenough, C. Xu, and H. D. Zhou, Phys. Rev. Lett. **107**, 197204 (2011).
[14] D. C. Johnston, Adv. Phys. **59**, 803 (2010).
[15] G. R. Stewart, Rev. Mod. Phys. **83**, 1589 (2011).
[16] P. Dai, Rev. Mod. Phys. **87**, 855 (2015).
[17] F.-C. Hsu, J.-Y. Luo, K.-W. Yeh, T.-K. Chen, T.-W. Huang, P. M. Wu, Y.-C. Lee, Y.-L. Huang, Y.-Y. Chu, D.-C. Yan *et al.*, Proc. Natl. Acad. Sci. USA **105**, 14262 (2008).
[18] P. A. Lee, N. Nagaosa, and X.-G. Wen, Rev. Mod. Phys. **78**, 17 (2006).
[19] T. M. McQueen, A. J. Williams, P. W. Stephens, J. Tao, Y. Zhu, V. Ksenofontov, F. Casper, C. Felser, and R. J. Cava, Phys. Rev. Lett. **103**, 057002 (2009).
[20] S. Medvedev, T. McQueen, I. Troyan, T. Palasyuk, M. Eremets, R. Cava, S. Naghavi, F. Casper, V. Ksenofontov, G. Wortmann *et al.*, Nat. Mater. **8**, 630 (2009).
[21] T. Shimojima, Y. Suzuki, T. Sonobe, A. Nakamura, M. Sakano, J. Omachi, K. Yoshioka, M. Kuwata-Gonokami, K. Ono, H. Kumigashira *et al.*, Phys. Rev. B **90**, 121111 (2014).
[22] K. Nakayama, Y. Miyata, G. N. Phan, T. Sato, Y. Tanabe, T. Urata, K. Tanigaki, and T. Takahashi, Phys. Rev. Lett. **113**, 237001 (2014).
[23] M. C. Rahn, R. A. Ewings, S. J. Sedlmaier, S. J. Clarke, and A. T. Boothroyd, Phys. Rev. B **91**, 180501 (2015).
[24] Q. Wang, Y. Shen, B. Pan, Y. Hao, M. Ma, F. Zhou, P. Steffens, K. Schmalzl, T. Forrest, M. Abdel-Hafiez *et al.*, Nat. Mater. **15**, 159 (2015).
[25] Q. Wang, Y. Shen, B. Pan, X. Zhang, K. Ikeuchi, K. Iida, A. D. Christianson, H. C. Walker, D. T. Adroja, M. Abdel-Hafiez *et al.*, Nat. Commun. **7**, 12182 (2016).
[26] A. E. Böhmer, T. Arai, F. Hardy, T. Hattori, T. Iye, T. Wolf, H. v. Löhneysen, K. Ishida, and C. Meingast, Phys. Rev. Lett. **114**, 027001 (2015).
[27] S. Baek, D. Efremov, J. Ok, J. Kim, J. van den Brink, and B. Büchner, Nat. Mater. **14**, 210 (2015).
[28] M. D. Watson, T. K. Kim, A. A. Haghighirad, N. R. Davies, A. McCollam, A. Narayanan, S. F. Blake, Y. L. Chen, S. Ghannadzadeh, A. J. Schofield *et al.*, Phys. Rev. B **91**, 155106 (2015).

[29] M. D. Watson, T. K. Kim, A. A. Haghighirad, S. F. Blake, N. R. Davies, M. Hoesch, T. Wolf, and A. I. Coldea, Phys. Rev. B **92**, 121108 (2015).

[30] P. Massat, D. Farina, I. Paul, S. Karlsson, P. Strobel, P. Toulemonde, M.-A. Measson, M. Cazayous, A. Sacuto, S. Kasahara *et al.*, Proc. Natl. Acad. Sci. USA **113**, 9177 (2016).

[31] T. Terashima, N. Kikugawa, A. Kiswandhi, D. Graf, E.-S. Choi, J. S. Brooks, S. Kasahara, T. Watashige, Y. Matsuda, T. Shibauchi *et al.*, Phys. Rev. B **93**, 094505 (2016).

[32] K. Kothapalli, A. E. Böhmer, W. T. Jayasekara, B. G. Ueland, P. Das, A. Sapkota, V. Taufour, Y. Xiao, E. Alp, S. L. Bud'ko *et al.*, Nat. Commun. **7**, 12728 (2016).

[33] P. S. Wang, S. S. Sun, Y. Cui, W. H. Song, T. R. Li, R. Yu, H. Lei, and W. Yu, Phys. Rev. Lett. **117**, 237001 (2016).

[34] L. Fanfarillo, J. Mansart, P. Toulemonde, H. Cercellier, P. Le Févre, F. Bertran, B. Valenzuela, L. Benfatto, and V. Brouet, Phys. Rev. B **94**, 155138 (2016).

[35] A. V. Chubukov, R. M. Fernandes, and J. Schmalian, Phys. Rev. B **91**, 201105 (2015).

[36] J. Glasbrenner, I. Mazin, H. O. Jeschke, P. Hirschfeld, R. Fernandes, and R. Valentí, Nat. Phys. **11**, 953 (2015).

[37] S. Wang and F. Wang, arXiv:1510.05476.

[38] F. Wang, S. A. Kivelson, and D.-H. Lee, Nat. Phys. **11**, 959 (2015).

[39] R. Yu and Q. Si, Phys. Rev. Lett. **115**, 116401 (2015).

[40] H.-H. Lai, W.-J. Hu, E. M. Nica, R. Yu, and Q. Si, Phys. Rev. Lett. **118**, 176401 (2017).

[41] Z. Wang, W.-J. Hu, and A. H. Nevidomskyy, Phys. Rev. Lett. **116**, 247203 (2016).

[42] C. Luo, T. Datta, and D.-X. Yao, Phys. Rev. B **93**, 235148 (2016).

[43] B. Busemeyer, M. Dagrada, S. Sorella, M. Casula, and L. K. Wagner, Phys. Rev. B **94**, 035108 (2016).

[44] H.-F. Zhu, H.-Y. Cao, Y. Xie, Y.-S. Hou, S. Chen, H. Xiang, and X.-G. Gong, Phys. Rev. B **93**, 024511 (2016).

[45] W. Z. Zhuo, M. H. Qin, S. Dong, X. G. Li, and J.-M. Liu, Phys. Rev. B **93**, 094424 (2016).

[46] H.-Y. Cao, S. Chen, H. Xiang, and X.-G. Gong, Phys. Rev. B **91**, 020504 (2015).

[47] A. L. Wysocki, K. D. Belashchenko, and V. P. Antropov, Nat. Phys. **7**, 485 (2011).

[48] J. Hu, B. Xu, W. Liu, N.-N. Hao, and Y. Wang, Phys. Rev. B **85**, 144403 (2012).

[49] R. Yu, Z. Wang, P. Goswami, A. H. Nevidomskyy, Q. Si, and E. Abrahams, Phys. Rev. B **86**, 085148 (2012).

[50] J. K. Glasbrenner, J. P. Velev, and I. I. Mazin, Phys. Rev. B **89**, 064509 (2014).

[51] D. Stanek, O. P. Sushkov, and G. S. Uhrig, Phys. Rev. B **84**, 064505 (2011).

[52] P. Bilbao Ergueta and A. H. Nevidomskyy, Phys. Rev. B **92**, 165102 (2015).

[53] H. C. Jiang, F. Krüger, J. E. Moore, D. N. Sheng, J. Zaanen, and Z. Y. Weng, Phys. Rev. B **79**, 174409 (2009).

[54] N. Read and S. Sachdev, Phys. Rev. Lett. **62**, 1694 (1989).

[55] N. Read and S. Sachdev, Phys. Rev. B **42**, 4568 (1990).

[56] N. Read and S. Sachdev, Phys. Rev. Lett. **66**, 1773 (1991).

[57] S. R. White, Phys. Rev. Lett. **69**, 2863 (1992).

[58] The ground-state energy for the magnetic and quadrupolar states obtained from the site-factorized wave function calculations can be found in the Supplemental Material of Ref. [39].

[59] I. McCulloch and M. Gulácsi, Europhys. Lett. **57**, 852 (2002).

[60] S. R. White and A. L. Chernyshev, Phys. Rev. Lett. **99**, 127004 (2007).

[61] S.-S. Gong, D. N. Sheng, O. I. Motrunich, and M. P. A. Fisher, Phys. Rev. B **88**, 165138 (2013).

[62] S.-S. Gong, W. Zhu, D. N. Sheng, O. I. Motrunich, and M. P. A. Fisher, Phys. Rev. Lett. **113**, 027201 (2014).

[63] A. W. Sandvik, Phys. Rev. B **85**, 134407 (2012).

[64] Z. Zhu, D. A. Huse, and S. R. White, Phys. Rev. Lett. **110**, 127205 (2013).

[65] Z. Zhu and S. R. White, Phys. Rev. B **92**, 041105 (2015).

[66] W.-J. Hu, S.-S. Gong, W. Zhu, and D. N. Sheng, Phys. Rev. B **92**, 140403 (2015).

[67] S. N. Saadatmand and I. P. McCulloch, Phys. Rev. B **94**, 121111 (2016).

[68] S. Yan, D. A. Huse, and S. R. White, Science **332**, 1173 (2011).

[69] S.-S. Gong, W. Zhu, and D. N. Sheng, Phys. Rev. B **92**, 195110 (2015).

[70] J. Towns, T. Cockerill, M. Dahan, I. Foster, K. Gaither, A. Grimshaw, V. Hazlewood, S. Lathrop, D. Lifka, G. D. Peterson *et al.*, Comput. Sci. Eng. **16**, 62 (2014).

[71] C. Lacroix, P. Mendels, and F. Mila, *Introduction to Frustrated Magnetism* (Springer Science & Business Media, New York, 2011).

[72] C. Kittel, Phys. Rev. **120**, 335 (1960).

[73] S. Raghu, X.-L. Qi, C.-X. Liu, D. J. Scalapino, and S.-C. Zhang, Phys. Rev. B **77**, 220503 (2008).

[74] P. Fazekas, *Lecture Notes on Electron Correlation and Magnetism* (World Scientific, Singapore, 1999).